

Parallel photonic reservoir computing based on frequency multiplexing of neurons.

Lorenz Butschek^{*1}, Akram Akrou¹, Evangelia Dimitriadou¹, Marc Haelterman², and Serge Massar^{†1}

¹Laboratoire d'Information Quantique, CP 224, Université libre de Bruxelles, Av. F. D. Roosevelt 50, B-1050, Bruxelles, Belgium

²OPERA-Photonique, CP 194/5, Université libre de Bruxelles, Av. F. D. Roosevelt 50, B-1050, Bruxelles, Belgium

August 2020

Abstract

Photonic implementations of reservoir computing can achieve state-of-the-art performance on a number of benchmark tasks, but are predominantly based on sequential data processing. Here we report a parallel implementation that uses frequency domain multiplexing of neuron states, with the potential of significantly reducing the computation time compared to sequential architectures. We illustrate its performance on two standard benchmark tasks. The present work represents an important advance towards high speed, low footprint, all optical photonic information processing.

1 Introduction

Reservoir Computing (RC) is a bio-inspired computational paradigm [1–3], that performs remarkably well for time-dependent signal processing. It has been applied to tasks such as speech recognition, nonlinear channel equalization, detection of epileptic seizures, time series prediction, etc., see the reviews [4, 5]. A reservoir computer is made of a large number of interconnected nodes, also called neurons or internal variables. This network, the reservoir, contains feedback connections and therefore behaves as a recurrent dynamical system. It is driven by the time dependent input signal. The reservoir output is a linear combination of the individual node states whose

^{*}lorenz.butschek@ulb.ac.be

[†]smassar@ulb.ac.be

weights are trained to optimize performance. In addition, adjusting some global system parameters can further optimize performance. However, unlike a traditional neural network the interconnection weights between nodes in a reservoir computer are not tuned individually, which greatly simplifies the training procedure and enables realization in physical systems.

During the last decade, several physical implementations of RC have been reported [6–21]. Of particular interest are the photonics-based reservoir computers, thanks to the remarkable speed and multiplexing capabilities of optical components. These were first proposed in [22, 23], and a number of experimental demonstrations have since been reported [7–18]. These are part of the wider current effort devoted to developing efficient photonic neural networks, see e.g. [24–28]

Many of the photonic reservoir computing experiments are based on a specific architecture consisting of a single nonlinear node with delayed feedback, first introduced using an electronic system in [6], see also the related theoretical proposal [29, 30]. In these systems, the delayed feedback is realized by a fiber loop and neurons propagate sequentially through the loop, amounting to time domain multiplexing of the neuron states. With this approach it is possible to build photonic reservoir computers that can solve, with error rates comparable to digital implementations, real world tasks such as speech recognition, time series prediction or channel equalization.

However the experimental reservoir computers based on time domain multiplexing suffer from an inherent trade-off between the number of neurons and the processing time. Indeed, adding more neurons to a time domain multiplexed system requires either increasing the length of the feedback loop or increasing the modulation frequency of the input signal. Because the input signal’s modulation frequency is ultimately limited by the input and read-out electronics, the solution is to lengthen the feedback loop, thereby increasing the total processing time. But light has multiple degrees of freedom: polarisation, frequency, space. By multiplexing the neurons in one of these domains, one can circumvent the above tradeoffs, and process multiple neurons simultaneously. Thus for instance, if one supposes that the ultimate speed limit is imposed by the input and read-out electronics, then a RC that processes 100 neurons in parallel would be 100 times faster than a sequential reservoir. For this reason recent efforts have focused on developing parallel photonic reservoirs where all the neurons are processed simultaneously, see [11, 15, 16]. However these experiments either did not perform very complex tasks, or were quite slow.

Here, we present a parallel photonic reservoir computer in which the reservoir states are encoded in the amplitude and phase of the frequency sidebands of a narrow band laser propagating in a single-mode, polarization-maintaining fiber optical loop. Frequency multiplexing is widely used in the telecommunication industry to increase the bandwidth of a communication channel such as an optical fiber. In our experiment the sidebands are created

and manipulated using an electro-optic phase modulator driven by a radio frequency signal, following ideas and techniques introduced in quantum optics [31, 32]. Our setup, following [11, 12], uses coherent optics and a linear optical network, with the nonlinearity implemented by the quadratic relation between the current generated in the read-out photodiode and the amplitude of the optical electric field. We evaluate performance on benchmark tasks often used in the reservoir computing community, obtaining results comparable to the state of the art. (An unpublished version of the present setup, but using fewer sidebands, can be found at [33]). The present results constitute an important step on the path towards development of high performance high-speed parallel optical reservoir computers. In the conclusion we discuss the potential for an integrated version of the present experiment.

2 Principle of operation and experimental setup

The fiber optics experimental setup is depicted in Fig. 1(a). The input of the reservoir is a time series $u(n)$ with $n \in \mathbb{N}$ denoting discrete time. The input is transformed into a function of continuous time t using a sample and hold procedure $u(t) = u(n)$ when $t \in [n\tau, (n+1)\tau[$, with the hold time τ equal to the roundtrip time of the cavity. The light source is a C-band continuous wave (CW) narrow band laser propagating in a single-mode fiber. The wavelength $\lambda = 2\pi c/\omega$ of the laser can be both temperature tuned in the range [1554.5, 1555.5] nm and piezo-tuned (with a response of 0.1 pm/V below 10 kHz). The piezo tuning is used to fix the cavity roundtrip phase to a given setpoint. A Mach Zehnder (MZ) lithium niobate modulator encodes the input $u(t)$, thereby producing the light amplitude

$$E(t) = E_0 \sin(\beta u(t) + \pi/4) e^{-i\omega t} \quad (1)$$

where we take into account the transfer function of the MZ modulator.

Frequency mixing is carried out by Phase Modulators (PM) driven by a radio frequency (RF) source at angular frequency Ω , thereby creating a frequency comb with separation $\Omega/2\pi$. Indeed such a PM acts on a monochromatic CW laser according to

$$\begin{aligned} E_0 e^{-i\omega t} &\rightarrow E_0 e^{-i\omega t} e^{-im \sin(\Omega t)} \\ &= E_0 e^{-i\omega t} \sum_k i^k J_k(m) e^{-ik\Omega t} \end{aligned} \quad (2)$$

where we have used the Jacobi-Anger expansion, with $J_k(m)$ the k -th order Bessel functions of the first kind, and $m = \pi V/V_\pi$ with V the applied voltage and V_π the characteristic voltage of the PM. Experimentally we vary the frequency $\Omega/2\pi$ in the range 15 – 18 GHz.

After encoding the input, a first phase modulator (PM1) driven with a high power RF amplifier A1 (33 dbm output power, corresponding to $m_1 =$

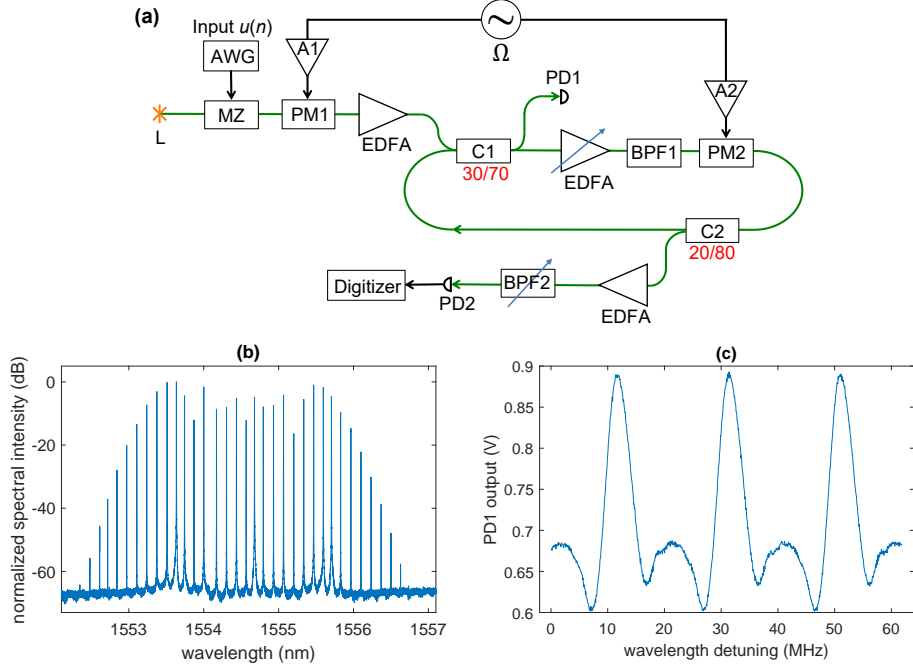


Figure 1: (a) Schematic of the experiment. The setup includes a Laser (L), an Arbitrary Waveform Generator (AWG) and Mach Zehnder Modulator (MZ) to encode the input, Phase Modulators (PM1 and PM2) driven by a RF source at frequency Ω amplified using amplifiers A1 and A2, Erbium Doped Fiber Amplifiers (EDFA), Couplers (C1 and C2), Band Pass Filters (BPF1 and BPF2), Photodiodes (PD1 and PD2). Optical fiber is represented in green, RF cables in black. Blue arrows denote tunable components. The output of PD1 is sent to a PID (not represented) that controls the frequency ω_0 of the laser L. A tap photodiode after the MZ (not represented) is used to fix the operating point of the MZ. (b) Measured frequency comb. In blue the spectrum measured at the output of PM1 with the input $u(t) = 0$ set to zero. (c) Example of transfer function of the experimental setup as a function of the laser wavelength shift. The vertical axis is the output of photodiode PD1 when the input $u(t) = 0$ is set to zero. In both panels the center wavelength is $\lambda = 1554.6$ nm and the RF modulation frequency $\Omega = 16.97632$ GHz. Note that in the right panel, the setpoint of the PID can be set in the ranges $[0.61, 0.63]$ V and $[0.68, 0.88]$ V. PID settings outside these ranges would correspond to either no or multiple values of the roundtrip phase. However, the transfer function changes considerably when Ω is scanned (see Section 5).

9.8) creates a wide optical comb at the input of the reservoir, see Fig. 1(b). After encoding the input and creating the frequency comb with PM1, a first Erbium Doped Fiber Amplifier (EDFA) boosts the optical power to approximately 17 dbm . This is then injected into the reservoir using the 30/70 coupler C1. The reservoir consists of an optical cavity with roundtrip time $\tau = 49.5$ ns corresponding to a Free Spectral Range of 20.2 MHz. The cavity itself contains a second PM (PM2) driven by RF amplifier A2 (20 dbm output power, corresponding to $m_2 = 2.2$), an EDFA with adjustable gain, a Band Pass Filter (BPF1) with 3 nm bandwidth in order to remove amplified spontaneous emission noise, and an output 20/80 tap coupler C2. The role of the intracavity PM is to mix frequencies within the cavity, thereby enriching the dynamics. The intracavity EDFA partially compensates the losses due to the intracavity optical components; its gain therefore determines the memory of the reservoir.

The input of the reservoir is a time series $u(n)$ with $n \in \mathbb{N}$ denoting discrete time. The input is transformed into a function of continuous time t using a sample and hold procedure $u(t) = u(n)$ when $t \in [n\tau, (n+1)\tau[$, with the hold time τ equal to the roundtrip time of the cavity. The Mach Zehnder (MZ) Modulator encodes the input on the optical field as

$$E_0 e^{-i\omega t} \rightarrow E_0 \sin(\beta u(t) + \pi/4) e^{-i\omega t} \quad (3)$$

where the sin takes into account the transfer function of the MZ modulator, and the factor β denotes the input amplitude depending on the driving voltage of the Arbitrary Waveform Generator (AWG).

As a consequence of this sample and hold procedure synchronized with the roundtrip time, we can express the whole dynamics in discrete time n . Indeed during the interval $t \in [n\tau, (n+1)\tau[$ of duration τ , the field amplitude at the output of the reservoir can be written as $E(t) = E e^{-i\omega t} \sum_k x_k(n) e^{-ik\Omega t}$ since the amplitudes $x_k(t) = x_k(n)$ of sideband k are constant during this interval.

Propagation through a Phase Modulator is then given by the matrix multiplication

$$\mathbf{x} \rightarrow \mathbf{J}\mathbf{x} \quad (4)$$

where $\mathbf{J} = (J_{jk})$ has components $J_{jk} = i^{j-k} J_{j-k}(m)$; while propagation through other optical components or optical fiber is given by multiplication by the diagonal matrix

$$\mathbf{x} \rightarrow \mathbf{\Phi}\mathbf{x} \quad (5)$$

with $\mathbf{\Phi}$ the diagonal matrix

$$\mathbf{\Phi} = (\Phi_{jk}) \quad , \quad \Phi_{jk} = \delta_{jk} e^{i\varphi(\omega, k)} . \quad (6)$$

Here δ_{jk} is the Kronecker delta and $\varphi(\omega, k)$ is the phase accumulated by sideband k as it passes through the optical component.

As a consequence the amplitude at the output of the reservoir is given by the linear recurrence

$$\begin{aligned}\mathbf{x}(n) = & \alpha \mathbf{\Phi}_3 \mathbf{J}(m_2) \mathbf{\Phi}_2 \mathbf{x}(n-1) \\ & + \mathbf{\Phi}_1 \mathbf{w}_{\text{in}}(m_1) \sin(\beta u(n) + \pi/4)\end{aligned}\quad (7)$$

where α is the amplitude damping of the cavity, $\mathbf{w}_{\text{in}}(m_1) = (J_{j0}(m_1))$ is the frequency comb due to phase modulator PM1, m_1 and m_2 are the parameters of the Phase Modulators PM1 and PM2, and $\mathbf{\Phi}_{1,2,3}$ describe the propagation from PM1 to coupler C1, from C1 to PM2, and from PM2 to C1 respectively.

Note that Eq. (7) is linear in \mathbf{x} . For this reason all optical losses and gains (due to the amplifiers) can be regrouped in the single parameter α .

Redefining $\mathbf{x}' = \mathbf{\Phi}_1^{-1} \mathbf{x}$, we have

$$\begin{aligned}\mathbf{x}'(n) = & \alpha \mathbf{\Phi}_3 \mathbf{J}(m_2) \mathbf{\Phi}_2 \mathbf{\Phi}_1 \mathbf{x}'(n-1) \\ & + \mathbf{w}_{\text{in}}(m_1) \sin(\beta u(n))\end{aligned}\quad (8)$$

which shows that the evolution equations in fact only depend on two propagation matrices ($\mathbf{\Phi}_3$ and the product $\mathbf{\Phi}_2 \mathbf{\Phi}_1$).

The output variables are the intensities of each sideband

$$I_k(n) = |x_k(n)|^2. \quad (9)$$

The output of the reservoir is a linear combination of the measured intensities

$$y(n) = \sum_k w_k I_k(n) \quad (10)$$

where the output weights w_k are adjusted in a postprocessing phase to minimize the Normalized Mean Square Error (NMSE) between the reservoir output $y(n)$ and the desired output $\bar{y}(n)$:

$$\text{NMSE} = \frac{\langle (\bar{y}(n) - y(n))^2 \rangle_n}{\langle (\bar{y}(n) - \langle \bar{y}(n) \rangle_n)^2 \rangle_n}. \quad (11)$$

Experimentally, sideband intensities are measured as follows: The output of C2 is reamplified by a readout EDFA from approximately 2.3 dbm to 12.4 dbm and sent to a tunable band pass filter (BPF2, Finisar Waveshaper, FWHM = 10 GHz), which is tuned to be centred on frequency bin $\omega + k\Omega$. The output of BPF2 is sent to PhotoDiode PD2 that records the intensity $I_k(n) = |x_k(n)|^2$ of each frequency bin at discrete time n . Because BPF2 only has 4 output ports, each intensity time series $I_k(n)$ is recorded sequentially, in a separate run of the experiment.

3 Numerical simulations

We have carried out detailed numerical simulations to validate our experimental results. These simulations are based on the discrete time model of section 3. Here we provide some additional details on the simulations.

We do not know the values of the matrices $\Phi_{1,2,3}$ in Eq. (8). For simplicity we set $\Phi_1 = \Phi_2 = \mathbf{I}$ to be the identity matrix. This allows us to investigate the consequences of varying the frequency Ω of the modulation without increasing the number of free parameters. (We have checked that this simplification does not affect the predictions of the simulations). That is we use the simplified dynamics

$$\mathbf{x}(n) = \alpha \Phi \mathbf{J}(m_2) \mathbf{x}(n-1) + \mathbf{w}_{\text{in}}(m_1) \sin(\beta u(n)) . \quad (12)$$

We also do not know the values of the phases $\varphi(\omega, k)$ that make up the matrix Φ in Eq. (12). In numerical simulations we use for $\varphi(\omega, k)$ the Sellmeier equation for single mode fiber. However, results with a linearized version of Eq. (6), using

$$\varphi(\omega, k) = \beta_0 L + \beta_1 L(\omega - \omega_0) + \beta_1 L \Omega k \quad (13)$$

show negligible differences, where β_0 is the zero-order propagation constant, $\beta_1 = v_g^{-1}$ is the inverse of the group velocity, L is the cavity length and $\omega - \omega_0$ is the detuning of the laser with respect to the reference frequency ω_0 . The round trip phase at the laser frequency ($k = 0$) is denoted $\varphi(\omega) = \beta_0 L + \beta_1(\omega - \omega_0)L$. Note that $L = \tau v_g$ with τ the roundtrip time, thus the parameter $\beta_1 L = \tau$. Experimentally we have $\tau = 49.5$ ns, which explains the very high sensitivity to $\omega - \omega_0$ and to Ω . A shorter cavity would considerably decrease this sensitivity.

The simulations also include the effect of phase noise in the cavity (by adding a noise term to $\varphi(\omega, k)$ as well as detection noise (by adding a noise term to Eq. (9)).

The key parameters that are varied in simulation are the feedback strength α , the frequency Ω of the modulation (which affects the matrix Φ), the input amplitude β . The driving strengths of the phase modulators (m_1 and m_2) can also be varied but are generally set to the maximum values possible.

4 Stabilisation and noise

Even with the input $u(t) = 0$ set to zero, this system constitutes a highly complex interferometer in the frequency domain. As illustrated in Fig. 1(b) more than 30 frequency bins interfere together. Each frequency bin accumulates a different phase $\varphi(k)$ during one round trip of the cavity. The phases $\varphi(k)$ are controlled in two ways. First we scan Ω with high precision. Second, for fixed Ω we stabilise the cavity as follows: the intensity

measured by photodiode PD1 is sent to a Proportional-Integral-Derivative (PID) controller (Toptica Digilock) whose output controls the wavelength λ of the laser through its piezo controller according to a given setpoint. An example transfer function of the cavity is plotted in Fig. 1(c), but note that they change significantly with Ω , see Section 5. We have found that the best setpoints are those where the intensity measured by PD1 is low. We believe that this is in part due to the fact that in this regime the intracavity intensity is higher, and therefore the intracavity EDFA is closer to saturation which leads to less spontaneous emission noise.

The experiment is highly sensitive to acoustic and electronic noise. Because of the intracavity EDFA and the RF connection to the intracavity phase modulator PM2 the optical cavity cannot be completely isolated from acoustic noise. As a consequence, even with the PID in operation, there is some residual acoustic noise present.

In addition the output RF amplifier A1 has a small low frequency (7.5 kHz) periodic component which we were unable to filter out. This low frequency component modulates the amplitude of the carrier and sidebands of the frequency comb. We synchronized all runs of the reservoir with this periodic noise in order to counteract its effect as much as possible. (The idea is similar to that exposed in [34]: the effect of a low frequency noise on reservoir performance can be mitigated by training the reservoir while letting the noise vary).

Furthermore, there is spontaneous emission noise from the EDFAs, as well as electronic noise from the readout photodiode PD2 and quantization noise from the digitizer. Overall the Signal to Noise Ratio (SNR) in the current setup is approximately 20 dB, which is too small for good reservoir operation. We therefore record 1000 times each output intensity time series $I_k(n)$ and then use the average of these time series in Eq. (10), thereby increasing the SNR to approximately 35 dB.

5 Video of cavity transfer functions

In order to illustrate the complexity of the multi-frequency interferometer, we present as ancillary file a one-minute video of the cavity transfer function when the modulation frequency Ω is scanned while the input $u(t) = 0$ is set to zero. We scan Ω in the range [16.975, 16.978] GHz. For each value of Ω we scan the frequency detuning of the laser over a range of 60 MHz. The recorded trace is presented in the left pane. A sample screen shot of the left pane is presented in Fig 1c of the main text. As the video shows, the response function of the cavity gradually changes as Ω is scanned.

The transfer function of the cavity is sensitive to the input power as the average intracavity power determines the gain of the intracavity EDFA (because of gain saturation of the intracavity EDFA). To illustrate this we

present the curves of the left pane for 3 values of the input EDFA. At lower input pump power the intracavity EDFA is further from saturation, its gain is therefore larger. As a consequence the finesse of the cavity is higher (measured as the normalized ratio of the maximum to minimum power as λ is scanned) for lower input power. For low input power, for certain values of Ω one even almost reaches the lasing threshold.

The right pane shows the minimum of the transfer functions (i.e. the minimum of the curves in the left pane) as a function of Ω . This provides a synthetic overview of how the transfer function evolves when Ω is scanned. Note that the dip around $\Omega/2\pi = 16.9771$ GHz is slightly shifted for the three datasets. This is a consequence of a long-term drift of the clock providing the frequency reference for the RF generator. When the reservoir computer is running, we use the position of this dip as calibration of Ω (employing a least-squares optimization of a few transfer functions recorded around the dip).

6 Results

6.1 Nonlinear channel equalization task.

This is a telecommunication application widely used as a benchmark in the reservoir computing community, see e.g. [3, 7, 10, 12, 29]. The aim of this task is, given the channel output $u(n)$, to reconstruct the channel input $d(n)$. The channel inputs $d(n)$ are drawn randomly from $\{-3, -1, 1, 3\}$. First, the signal travels through a linear channel resulting in:

$$\begin{aligned} q(n) = & 0.08d(n+2) - 0.12d(n+1) + d(n) + 0.18d(n-1) \\ & - 0.1d(n-2) + 0.091d(n-3) - 0.05d(n-4) \\ & + 0.04d(n-5) + 0.03d(n-6) + 0.01d(n-7). \end{aligned}$$

Then it goes through a noisy nonlinear channel. The resulting outputs $u(n)$ are given by:

$$u(n) = q(n) + 0.036q^2(n) - 0.11q^3(n) + \nu(n) \quad (14)$$

where $\nu(n)$ is an additive zero-mean Gaussian noise which is adjusted in power to obtain a signal-to-noise ratio ranging from 12 dB to 32 dB. The signal $u(n)$ received at the end of the communication channel is used as the input of the reservoir computer. Then the reservoir is trained to generate the original sequence $d(n)$. The reservoir performances are evaluated by calculating the Symbol Error Rate (SER), defined by the fraction of the misclassified symbols within the generated sequence $d(n)$.

After a first sequence of 200 symbols used to remove transients, the reservoir is trained on a sequence of 2670 symbols, and then tested on 2470 symbols (synchronized to the 7.5 kHz periodic phase noise mentioned earlier).

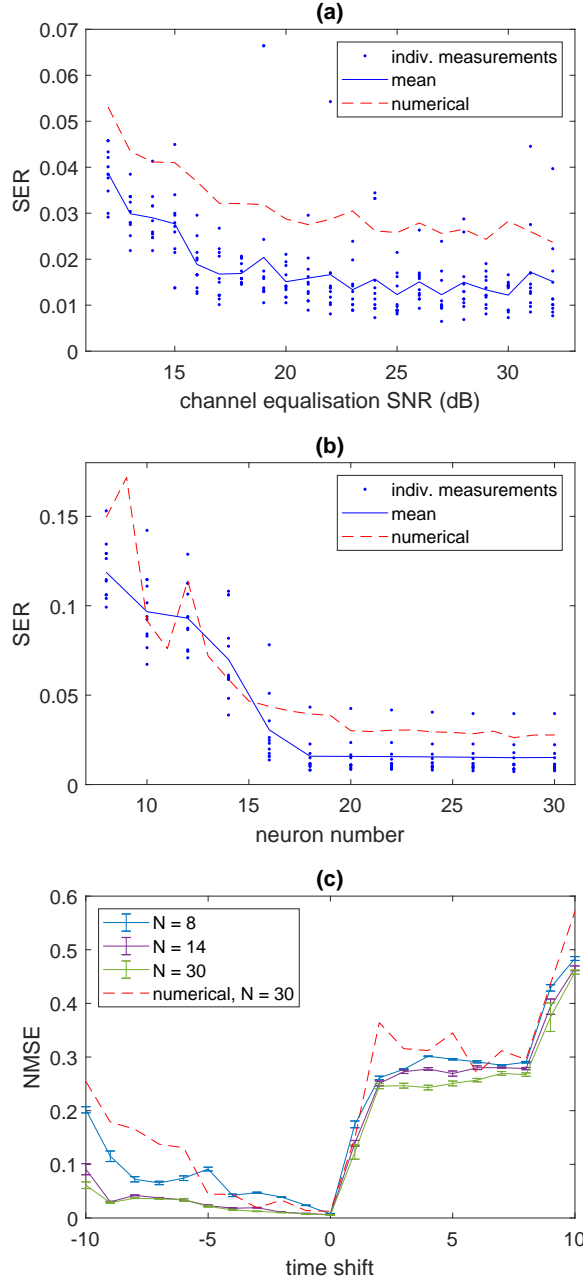


Figure 2: Results. Channel equalisation task: (a) Symbol Error Rate (SER) versus SNR for 30 neurons; (b) SER plotted against neuron number for fixed SNR of 30 dB. Note that numerical simulations (dashed line) suggest worse performance than the actual experiments (dots and solid line). Panel (c): SantaFe time series prediction of future inputs (positive shift) and recovery of past inputs (negative shift). Experimental results (error bars represent the standard deviation of 10 consecutive runs) for $N \in \{8, 14, 30\}$ again show better performance than numerical simulations (dashed line).

Results are plotted in Fig. 2(a) where the SER is plotted versus the SNR of the channel. The modulation frequency is $\Omega/2\pi=16.976\,32$ GHz. The feedback gain (see Supplementary Material I for the definition) is $\alpha=0.54$. The voltage amplitude of the input MZ is chosen such that the input intensity $\sin^2(\beta u(t) + \pi/4) \in [0.2, 0.8]$. Experimental results are better than the predictions of the numerical model. A possible explanation is a so far unknown nonlinear effect in the setup, as nonlinearities are known to boost performance for certain tasks.

In Fig. 2(b) we investigate the effect of the number of frequency bins used as neurons on the performance: we record the outputs of all 30 frequency bins; we then optimize the output while only using the central N frequency bins. We plot the SER for different values of N as a function of the SNR of the channel. We see that for this task performance improves significantly as N increases from $N=8$ to $N=18$ after which performance saturates.

6.2 Chaotic laser time series prediction.

Another widely used benchmark for reservoir computing is a time-series prediction of the recorded output of a chaotically operating far-infrared laser [35].

As in the previous task, the first 200 steps of the dataset are discarded as a warmup sequence, after which the training sequence consists of 2670 steps, followed by 2470 steps for testing. In this case the modulation frequency is $\Omega/2\pi=16.976\,21$ GHz, all other parameters are unchanged with respect to the channel equalization task. The performance of the reservoir to predict future inputs as well as recover past inputs for $N \in \{8, 14, 30\}$ can be seen in Fig. 2(c). At $N=30$ the one-step prediction error is $\text{NMSE}=0.123 \pm 0.01$. Conformity to numerical results is better than in the first task, but again the experiment outperforms them.

7 Conclusion

To continue improving computational devices one of the most promising approaches is to take inspiration from the biological brain, while exploiting the possibilities offered by modern technology. The present work does just that, by showing how reservoir computing, a brain inspired approach to computation, can be implemented with light using frequency multiplexing, a technique widely used in telecommunications. This offers a new route to developing compact, high performance, optical information processing.

An important goal towards the development of photonic neural networks is the realisation of integrated versions of the experiments, which enables considerable gain in footprint, cost, energy consumption, see [11, 18, 25] for recent advances in this direction. A preliminary study [36] suggests that it should be possible to integrate the present experiment on an InP chip, solving

many of the stabilisation problems which affect the present experiment. With an RF modulation frequency of $\Omega/2\pi=10$ GHz and a free spectral range of 2.5 GHz the system would be comparable to other integrated photonic neural networks.

Acknowledgements

The authors would like to thank Q. Vinckier and A. Bouwens for their contribution to an early version of this experiment. The authors acknowledge financial support by the FRS-FNRS grant PDR T.0089.18, and by the European Commission grant 860360-POSTDIGITAL.

References

- [1] H. Jaeger, Bonn, Germany: German National Research Center for Information Technology GMD Technical Report **148**, 13 (2001).
- [2] W. Maass, T. Natschläger, and H. Markram, Neural computation **14**, 2531 (2002).
- [3] H. Jaeger and H. Haas, science **304**, 78 (2004).
- [4] M. Lukoševičius and H. Jaeger, Computer Science Review **3**, 127 (2009).
- [5] M. Lukoševičius, H. Jaeger, and B. Schrauwen, KI-Künstliche Intelligenz **26**, 365 (2012).
- [6] L. Appeltant, M. C. Soriano, G. Van der Sande, J. Danckaert, S. Massar, J. Dambre, B. Schrauwen, C. R. Mirasso, and I. Fischer, Nature communications **2**, 1 (2011).
- [7] Y. Paquot, F. Duport, A. Smerieri, J. Dambre, B. Schrauwen, M. Haelterman, and S. Massar, Scientific reports **2**, 287 (2012).
- [8] L. Larger, M. C. Soriano, D. Brunner, L. Appeltant, J. M. Gutiérrez, L. Pesquera, C. R. Mirasso, and I. Fischer, Optics express **20**, 3241 (2012).
- [9] R. Martinenghi, S. Rybalko, M. Jacquot, Y. K. Chembo, and L. Larger, Physical review letters **108**, 244101 (2012).
- [10] F. Duport, B. Schneider, A. Smerieri, M. Haelterman, and S. Massar, Optics express **20**, 22783 (2012).
- [11] K. Vandoorne, P. Mechet, T. Van Vaerenbergh, M. Fiers, G. Morthier, D. Verstraeten, B. Schrauwen, J. Dambre, and P. Bienstman, Nature communications **5**, 1 (2014).

- [12] Q. Vinckier, F. Duport, A. Smerieri, K. Vandoorne, P. Bienstman, M. Haelterman, and S. Massar, *Optica* **2**, 438 (2015).
- [13] D. Brunner, M. C. Soriano, C. R. Mirasso, and I. Fischer, *Nature communications* **4**, 1 (2013).
- [14] L. Larger, A. Baylón-Fuentes, R. Martinenghi, V. S. Udaltsov, Y. K. Chembo, and M. Jacquot, *Physical Review X* **7**, 011015 (2017).
- [15] J. Bueno, S. Maktoobi, L. Froehly, I. Fischer, M. Jacquot, L. Larger, and D. Brunner, *Optica* **5**, 756 (2018).
- [16] P. Antonik, N. Marsal, D. Brunner, and D. Rontani, *Nature Machine Intelligence* **1**, 530 (2019).
- [17] J. Dong, M. Rafayelyan, F. Krzakala, and S. Gigan, *IEEE Journal of Selected Topics in Quantum Electronics* **26**, 1 (2019).
- [18] K. Harkhoe, G. Verschaffelt, A. Katumba, P. Bienstman, and G. Van der Sande, *Optics Express* **28**, 3086 (2020).
- [19] J. Torrejon, M. Riou, F. A. Araujo, S. Tsunegi, G. Khalsa, D. Querlioz, P. Bortolotti, V. Cros, K. Yakushiji, A. Fukushima, *et al.*, *Nature* **547**, 428 (2017).
- [20] C. Du, F. Cai, M. A. Zidan, W. Ma, S. H. Lee, and W. D. Lu, *Nature communications* **8**, 1 (2017).
- [21] G. Dion, S. Mejaouri, and J. Sylvestre, *Journal of Applied Physics* **124**, 152132 (2018).
- [22] K. Vandoorne, W. Dierckx, B. Schrauwen, D. Verstraeten, R. Baets, P. Bienstman, and J. Van Campenhout, *Optics express* **16**, 11182 (2008).
- [23] K. Vandoorne, J. Dambre, D. Verstraeten, B. Schrauwen, and P. Bienstman, *IEEE transactions on neural networks* **22**, 1469 (2011).
- [24] A. Saade, F. Caltagirone, I. Carron, L. Daudet, A. Drémeau, S. Gigan, and F. Krzakala, in *2016 IEEE International Conference on Acoustics, Speech and Signal Processing (ICASSP)* (IEEE, 2016) pp. 6215–6219.
- [25] Y. Shen, N. C. Harris, S. Skirlo, M. Prabhu, T. Baehr-Jones, M. Hochberg, X. Sun, S. Zhao, H. Larochelle, D. Englund, *et al.*, *Nature Photonics* **11**, 441 (2017).
- [26] X. Lin, Y. Rivenson, N. T. Yardimci, M. Veli, Y. Luo, M. Jarrahi, and A. Ozcan, *Science* **361**, 1004 (2018).

- [27] T. F. De Lima, H.-T. Peng, A. N. Tait, M. A. Nahmias, H. B. Miller, B. J. Shastri, and P. R. Prucnal, *Journal of Lightwave Technology* **37**, 1515 (2019).
- [28] J. Feldmann, N. Youngblood, C. D. Wright, H. Bhaskaran, and W. Pernice, *Nature* **569**, 208 (2019).
- [29] A. Rodan and P. Tiño, in *International Conference on Intelligent Data Engineering and Automated Learning* (Springer, 2010) pp. 267–274.
- [30] A. Rodan and P. Tino, *IEEE transactions on neural networks* **22**, 131 (2010).
- [31] M. Bloch, S. W. McLaughlin, J.-M. Merolla, and F. Patois, *Optics letters* **32**, 301 (2007).
- [32] L. Oslslager, J. Cussey, A. T. Nguyen, P. Emplit, S. Massar, J.-M. Merolla, and K. P. Huy, *Physical Review A* **82**, 013804 (2010).
- [33] A. Akrou, A. Bouwens, F. Duport, Q. Vinckier, M. Haelterman, and S. Massar, *arXiv preprint arXiv:1612.08606* (2016).
- [34] R. Alata, J. Pauwels, M. Haelterman, and S. Massar, *IEEE Journal of Selected Topics in Quantum Electronics* **26**, 1 (2019).
- [35] A. S. Weigend, *Time series prediction: forecasting the future and understanding the past* (Routledge, 2018).
- [36] W. Kassa, E. Dimitriadou, M. Haelterman, S. Massar, and E. Bente, in *Neuro-inspired Photonic Computing*, Vol. 10689 (International Society for Optics and Photonics, 2018) p. 1068903.